Hindawi

Research Article

Probe Sonicated Synthesis of Bismuth Oxide (Bi$_2$O$_3$): Photocatalytic Application and Electrochemical Sensing of Ascorbic Acid and Lead

K. B. Kusuma [iD],[1] **M. Manju** [iD],[2] **C. R. Ravikumar** [iD],[1] **V. G. Dileepkumar** [iD],[3] **A. Naveen Kumar** [iD],[1] **Mysore Sridhar Santosh** [iD],[3,4] **H. C. Ananda Murthy** [iD],[5] **and K. Gurushantha** [iD][6]

[1]*Research Center, Department of Science, East West Institute of Technology, V.T.U, -91, Bangalore, India*
[2]*Department of Chemistry, Sri Krishna Institute of Technology, VTU, -90, Bangalore, India*
[3]*Coal to Hydrogen Energy for Sustainable Solutions (CHESS), CSIR-Central Institute of Mining & Fuel Research (CIMFR), Digwadih Campus, PO: FRI, Dhanbad - 828 108, Jharkhand, India*
[4]*Academy of Scientific and Innovative Research (AcSIR), Ghaziabad - 201002, Uttar Pradesh, India*
[5]*Department of Applied Chemistry, School of Applied Natural Science, Adama Science and Technology University, PO Box 1888, Adama, Ethiopia*
[6]*Department of Chemistry, M S Ramaiah Institute of Technology, MSR Nagar, Bengaluru-560054, India*

Correspondence should be addressed to H. C. Ananda Murthy; anandkps350@gmail.com

A simple and low-cost and highly calibrated probe sonication method was used to prepare bismuth oxide nanoparticles (Bi$_2$O$_3$ NPs). The formation of a well-crystalline sample at the end of the product has been further calcined at 600°C for 2 hrs. The powder X-ray diffraction (PXRD) patterns of the NPs substantiated the monoclinic structure (space group P2$_1$/c), and the average crystallite size was found to be 60 nm, which was also confirmed by transmission electron microscopic (TEM) studies. Scanning electron microscopic (SEM) images depicted highly porous Bi$_2$O$_3$ NPs with little agglomeration. Utilizing diffused reflectance spectra (DRS) data, the energy bandgap (E_g) value of 3.3 eV was deduced for Bi$_2$O$_3$ NPs, and their semiconductor behavior has been confirmed. Two dyes, methylene blue (MB) and acid green (AG) were utilized for degradation studies using Bi$_2$O$_3$ NPs under UV light irradiation (from 0 to 120 min). The photocatalytic degradation was found to be maximum for MB (93.45%) and AR (97.80%) dyes. Cyclic voltammetric (CV) and sensor studies using the electrochemical impedance spectroscopy (EIS) were performed. The specific capacitance value of 25.5 Fg^{-1} was deduced from the cyclic voltammograms of the Bi$_2$O$_3$ electrode in 0.1 N HCl with a scan rate of 10 to 50 mV/s. From the obtained EIS data, the Bi$_2$O$_3$ electrode showed pseudocapacitive characteristics. The prepared electrodes also exhibited high sensitivity towards the detection of ascorbic acid and lead. Hence, sonochemically synthesized Bi$_2$O$_3$ NPs are possibly hopeful for excellent photocatalytic and electrochemical sensing of biomolecules.

1. Introduction

With the rapid escalation of industrial activities by mankind, environmental remediation of pollutants has become an issue of global concern. Many industries such as textile, food processing, pharmaceuticals, tannery, papermaking, and electro-plating are the source of dyes in the water bodies leading to the contamination of water [1, 2]. A significant amount of industrial waste is being released into the environment as the chemical industry grows, and this waste has a high likelihood of causing adverse reactions in human beings, such as immunological dysfunction and reproductive system abnormalities,
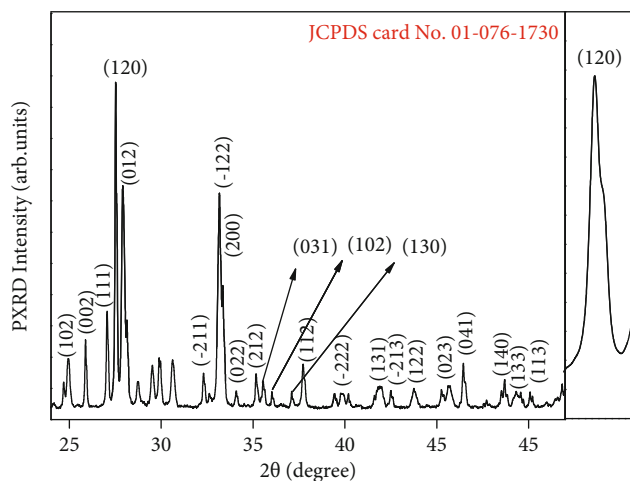
FIGURE 1: PXRD patterns of Bi_2O_3 NPs.

TABLE 1: FWHM values, d-spacing, and Miller indices for Bi_2O_3.

Miller indices (hkl)	2θ (degree)	FWHM (degree)	d-spacing (nm)	Crystal size (nm)
102	24.9	0.17	0.43	55.78
002	25.8	0.20	0.37	52.00
120	27.5	0.13	0.33	65.78
012	27.9	0.15	0.39	53.13
-122	33.1	0.19	0.40	63.11
212	35.2	0.14	0.32	59.21
112	37.6	0.16	0.35	60.14
041	46.4	0.21	0.42	61.21

Average crystallite size = 58.79 nm.

as well as neurological and behavioral abnormalities. Because the therapy or cure for many diseases, such as diabetes, is still in the early stages of development, it is critical to control the living conditions associated with the disease. The monitoring of heavy metals such as lead and monitoring of the drug ascorbic acid is necessary to induce the welfare of humans as well as water bodies. As a result, the development of novel sensors for the detection of substances at trace quantities has emerged as a highly essential area of research. Electrochemical detection methods have a number of advantages over other conventional procedures. Electrochemical sensors are one of the fields that are growing at the fastest rate. Amperometric sensors use the voltage difference between a reference and an electrode to cause the oxidation or reduction of an electroactive species in a reaction [3–6]. A large number of nanometal oxides have been applied to degrade many pollutant dyes for many decades [7].

There are numerous transition metal oxides such as ZnO, Mn_2O_3, Fe_3O_4, TiO_2, and Fe_2O_3, which have been applied to degrade the plenty of dye molecules [8–11]. Each of these metal oxides exhibits good degradation efficiency, but still face serious drawbacks such as fast electron-hole recombination, agglomeration, and inefficient band gap values. Thus, to find an alternative metal oxide for the effective photocatalytic degradation, Bi_2O_3 has been chosen in this work due to its environmental friendly applications in

solid oxide fuel cells, gas sensors, photocatalyst, energy, and medicine [12–14]. It is well known that bismuth oxide has six polymorphic forms, denoted by α-Bi_2O_3 (monoclinic), β-Bi_2O_3 (tetragonal), δ-Bi_2O_3 (face-centered cubic), γ-Bi_2O_3 (body-centered cubic), φ-Bi_2O_3 (orthorhombic), and Bi_2O_3 (triclinic), respectively [15, 16]. Among them, α- and δ-phases are stable both at low temperatures as well as at higher temperatures, respectively, but the others remain in a metastable phase at high temperatures Bi_2O_3 has a lot of peculiar physical and chemical properties, such as a wide energy gap change (from 2 to 3.96 eV), high metal oxide ion conductivity properties (1.0 s/cm), high refractive index, dielectric permittivity, addition to that, and excellent photo conductivities and photoluminescence properties [17, 18].

Modified nanoelectrodes have been utilized for the determination of paracetamol in pharmaceutical preparations including electrodeposition attachment of metal nanoparticles such as Au, Ru, and Cu. In addition, fullerene and carbon nanotube-based electrodes also showed high sensitivity with a low detection limit [19, 20]. Generally, the modification of the electrode is needed for a sensitive and selective determination of overdose levels of paracetamol in whole blood or urine samples [21–23]. Bismuth oxide NP modified carbon electrode has been employed for the determination of heavy metal ions present in drinking water, mineral water, and urine samples [24, 25]. The fabrication of chemically modified nanoelectrode (CMNE) has been widely used to improve the sensitivity and selectivity of amino acids, vitamins, drugs, DNA, and many more [26–28].

Many researchers have reported different methods for the synthesis of NPs, such as thermal decomposition using organic solvents which create hampers. The combustion method is one of the fast methods for the synthesis of NPs, but in the combustion method, it is difficult to control the agglomeration of the NPs. The other method for the fast and better yield is the coprecipitation method where there will be no control over the size distribution of the NPs. The probe-sonication method was proven to be the best due to its accuracy and capacity to form nanosized small particles. The synthesis of NPs by the application of ultrasonic waves exhibited various advantages like fast rate of reaction, high purity, and narrow distribution of particle sizes [29]. Several authors have reported the synthesis of many NPs through the sonochemical method.

In the present work, we aimed to synthesize Bi_2O_3 NPs by using the probe sonication method. This method is usually applied for the preparation of nanometal oxides. This method usually differs from other traditional procedures. In recent times, this method has also been applied to prepare binary metal oxides. Probe sonicationally synthesized powdered Bi_2O_3 nanomaterials using $Bi(NO_3)_3 \cdot 5H_2O$ offer many advantages like a good degree of crystallinity, well-established morphology, and high purity. After the calcination, the obtained pure powders of Bi_2O_3 NPs were characterized by the techniques like PXRD, FTIR, SEM, and TEM. To the best of our knowledge, no one has reported the improvement of electrocatalytic oxidation of paracetamol using nanoparticle bismuth oxide modified by graphite

TABLE 2: Estimated structural parameters of Bi_2O_3 NPs prepared from probe sonication method.

Plane for Bi_2O_3	$\beta \times 10^{-3}$	D (nm)	d (nm)	$V \times 10^{-30}$ m³	$n \times 10^{-21}$	Dx $\times 10^4$ (kgm⁻³)	$\delta \times 10^{15}$ (kgm⁻³)⁻²	$\varepsilon \times 10^{-3}$	E (GPa)	$\sigma \times 10^8$ (Pa)	SF
(120)	0.13	65.78	0.33	20.0	6.47	8.63	22.32	8.650	119.2	3.41	0.35
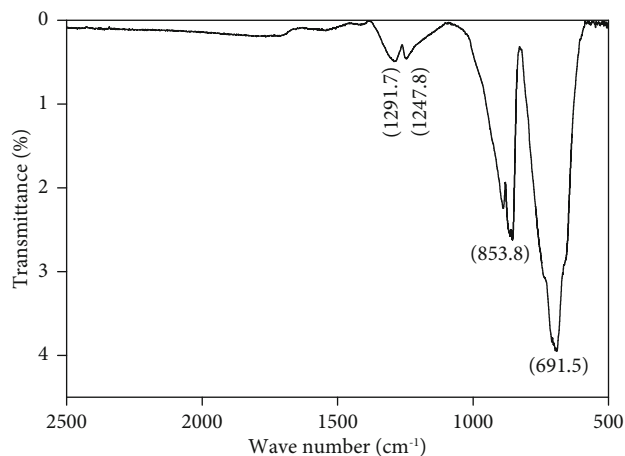
FIGURE 2: FT-IR spectrum of Bi_2O_3 NPs.

carbon electrode. The characterization of a known amount of Bi_2O_3 NPs that could catalyse the oxidation process of paracetamol in an acidic medium was investigated.

2. Experimental

2.1. Synthesis of Bismuth Oxide Nanoparticles (Bi_2O_3 NPs).
The synthesis of Bi_2O_3 NPs by probe sonication method from the precursors, bismuth nitrate pentahydrate (Bi $(NO_3)_3 \cdot 5H_2O$), and sodium hydroxide (NaOH) taken in the ratio of 1:2 was carried out with the support of ultrasound radiation. All the chemicals were used as received in analytical reagent (AR) grade. 1.0 M solution of bismuth nitrate pentahydrate (4.85 g) was added to a mixture of 5 mL of concentrated nitric acid (HNO_3) and 45 mL of deionized water with continuous stirring. Then, 0.5 M solution of sodium hydroxide (1 g) was added dropwise to the above precursor solution under stirring. This solution was bombarded with high-intensity ultrasound radiation at 40°C for 1 hr by using a microprocessor unit controlled ultrasonic probe of 13 mm diameter made up of high-grade titanium alloy (model PRO-550, 20 kHz, 500 W), operated at 20% amplitude, 20 kHz frequency with 100 W theoretical power dissipation [30]. On completion of the reaction process, a light yellow precipitate was formed. Then, the solution was centrifuged and the obtained precipitate was washed with distilled water and ethanol to remove excess NaOH. The precipitate was dried in a hot air oven at 100°C for 1 hr and calcined at 600°C for 2 hrs to get greenish coloured Bi_2O_3 NPs.

2.2. Instrumentation.
The structural analysis, functional group analysis, morphological studies, and optical analysis were carried out using, X-ray diffractometer (Shimadzu) (CuKα-1.541 Å) with a scan rate of 20 per minute, Perkin

Elmer FTIR (Spectrum-1000) spectrometer in the range of 4000-400 cm⁻¹, JEOL transmission electron microscopy (TEM) (JEM-2100 (accelerating voltage up to 200 kV, LaB6 filament)), and Shimadzu UV–Vis spectrophotometer model 2600 in the range of 200–800 nm, respectively. The cyclic voltammetric and impedance measurements were executed on an electrochemical analyzer CHI608E potentiostat and in a tri-electrode system.

2.3. Preparation of an Electrode from Carbon Paste.
The working electrode was made by blending Bi_2O_3 NPs with graphite powder (conducting carbon) and silicon oil (binder) in the weight ratio of 15:70:15 and made into a consistent slurry by physically grinding [31, 32]. Finely grounded material was filled into a teflon cavity tube (homemade) and confirming a fitted packing and the packed carbon paste surface was then smoothened.

3. Results and Discussion

3.1. Powder X-Ray Diffraction Studies.
Figure 1 reveals the PXRD patterns of Bi_2O_3 NPs synthesized by the probe sonication method and calcined at 600°C for 2 hrs. The diffraction peaks appeared at 2θ values of 24.9°, 25.8°, 27.4°, 27.9°, 33.1°, 35.2°, 37.6°, and 46.4° are correlated to (102), (002), (120), (012), (-122), (212), (112), and (041) planes which are very well indexed to monoclinic structure and in compliance with JCPDS card no. 01-076-1730 with phase group P2$_1$/c [33]. The lattice parameters were found to be; $a = 5.8499 Å$, $b = 8.1698 Å$, and $c = 7.5123 Å$ and $\alpha = 90°$, $\beta = 112.988°$, and $\gamma = 90°$. From Debye-Scherrer's formula (equation (1)), the crystallite size of Bi_2O_3 NPs was deduced to be in the range between 55 and 60 nm (Table 1).

$$D = \frac{k\lambda}{\beta \cos \theta}, \qquad (1)$$

where β is full width at half maximum (FWHM) of the diffraction peak, λ is wavelength of X-ray (1.5418 Å), θ is Bragg's angle, and k is Scherrer's constant (0.88–0.92); the average value of 0.9 was used for the calculation.

The d-spacing can be deduced using the following equation

$$\frac{1}{d^2} = \frac{1}{\sin^2 \beta} \left[\frac{h^2}{a^2} + \frac{k^2 \sin^2 \beta}{b^2} + \frac{l^2}{c^2} - \frac{2hl \cos \beta}{ac} \right], \qquad (2)$$
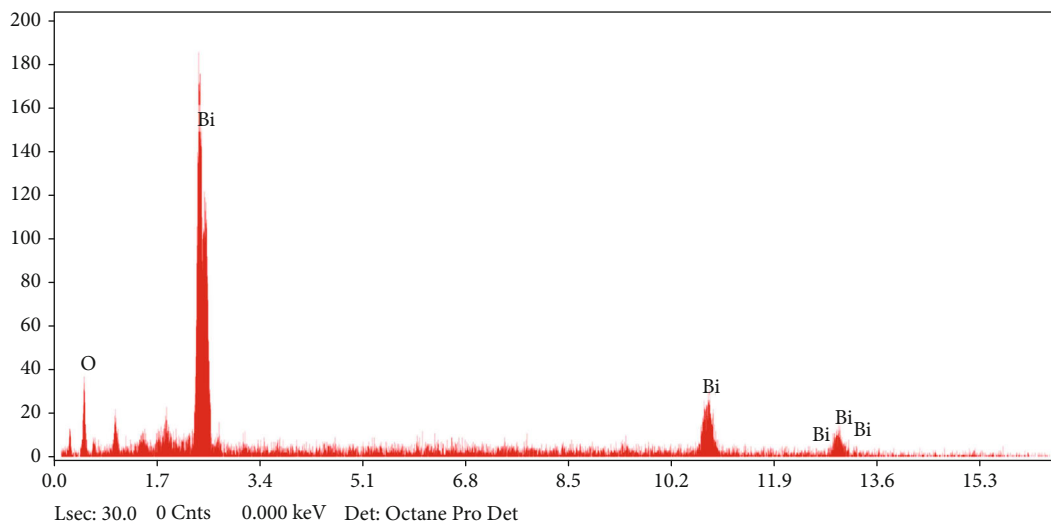
where a, b, and c are lattice parameters, $(h\,k\,l)$ is Miller indices, and d_{hkl} is interplanar spacing for $(h\,k\,l)$.

FWHM values, crystallite sizes, d-spacing values, and Miller indices for Bi_2O_3 NPs obtained from the probe sonication method have been tabulated in Table 1.
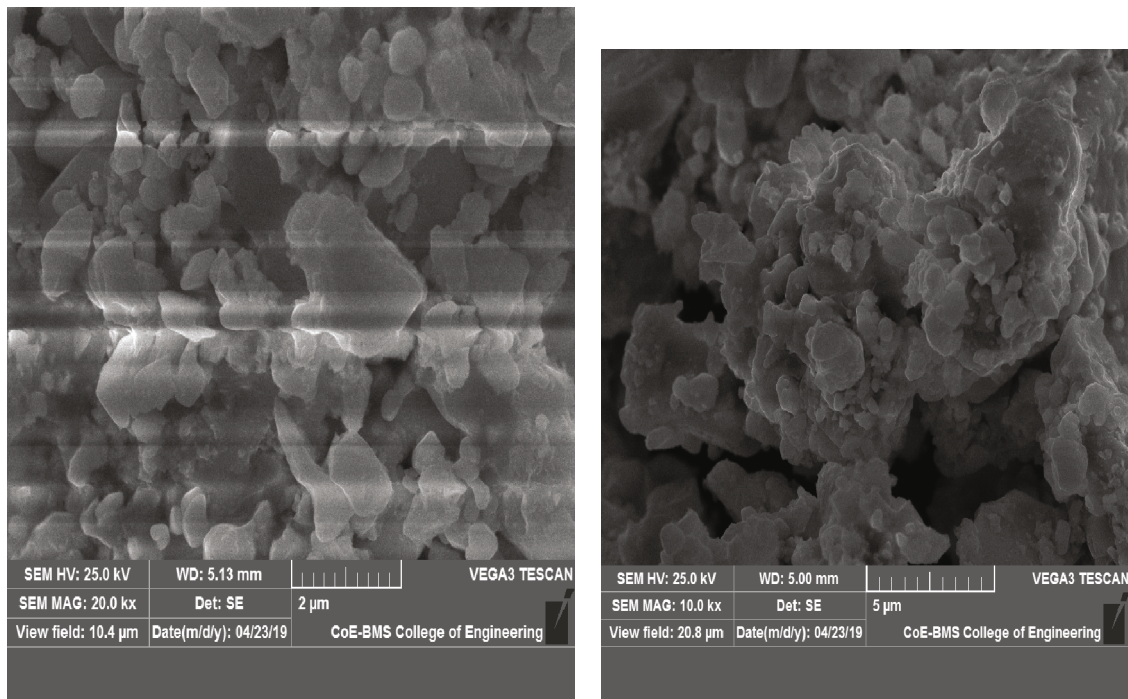
(a)

(b)

(c)

FIGURE 3: (a) and (b) SEM images. (c) EDAX of Bi_2O_3 NPs.

TABLE 3: Compositional data obtained from EDAX.

Element	Weight %	Atomic %
O K	15.09	69.89
Bi L	84.91	30.11

Various other crystal parameters such as unit cell volume (V), the number of unit cells (n), X-ray density (Dx), dislocation density (δ), microstrain (ε), stress (σ), and stacking fault were determined using PXRD data (Table 2) and following relationships [14, 21, 34]:

$$V = a^3, \tag{3}$$

$$N = \frac{4}{3\pi(D/2V)}, \tag{4}$$

$$Dx = \frac{16M}{Na^3}, \tag{5}$$

$$\delta = \frac{1}{D^2}, \tag{6}$$

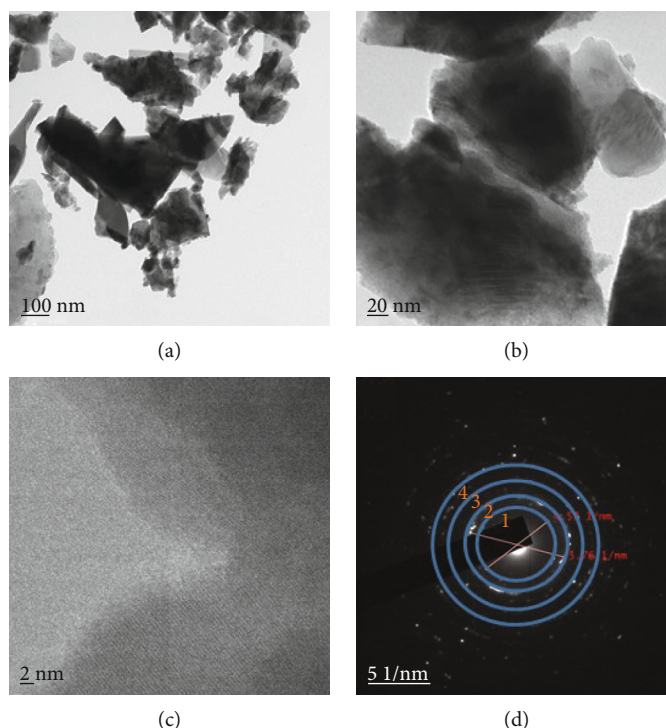$$\varepsilon = \frac{\beta \cos \theta}{4}, \tag{7}$$

(a)

(b)

(c)

(d)

FIGURE 4: (a) and (b) TEM images, (c) SAED pattern, and (d) HR-TEM of Bi_2O_3 NPs.
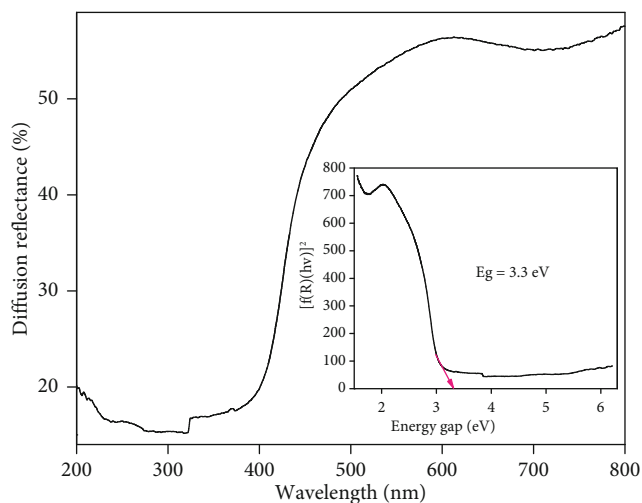

FIGURE 5: DRS and energy bandgap spectra patterns of Bi_2O_3 NPs.

$$\sigma stress = \epsilon E, \qquad (8)$$

$$S.F = \frac{2\pi^2}{45\sqrt{3}\tan\theta}, \qquad (9)$$

where M is molecular mass, N is Avogadro's number (6.0223×10^{23} particles mol^{-1}), and E is elastic constant of the material.

3.2. Fourier-Transform Infrared Spectroscopy. The Fourier transform infrared (FTIR) spectrum of Bi_2O_3 NPs was recorded in the wavenumber range of 400–4000 cm^{-1} at room temperature using KBr pellets Figure 2. The appear-

ance of two peaks at 691.5 cm^{-1} and 853.8 cm^{-1} corresponds to the metal-oxygen (Bi-O) vibration [35]. After calcination of Bi_2O_3 NPs at 500°C, many peaks were assumed to have disappeared because of the evaporation of most of the solvent molecules and decomposition of the organic ingredient. The additional peaks, at about 1291 cm^{-1} and 1247 cm^{-1}, can be attributed to $Bi^{3+}- O^{2-}$ stretching.

3.3. SEM Analysis. SEM micrographs of Bi_2O_3 NPs as shown in Figures 3(a) and 3(b) approve the formation of highly porous and agglomerated nanoparticles with an irregular morphology which is possibly due to the escape of a large amount of gases during the probe sonication process [36, 37]. These NPs were found to possess active surface sites and thus they can be suitably employed for applications in electrochemical and supercapacitor devices. The EDX spectrum of Bi_2O_3 NPs is presented in Figure 3(c). The spectrum confirmed the presence of only Bi and O elements (Table 3) in Bi_2O_3 NPs confirming the purity of the NPs.

3.4. TEM Analysis. The surface morphology of the synthesized Bi_2O_3 nanostructures was investigated using high-resolution transmission electron microscopy (HRTEM), and the morphology is depicted in Figure 4. Figures 4(a) and 4(b) show that the morphology has been slightly agglomerated, but SEM and TEM images show that the prepared Bi_2O_3 has a sheet shape morphology, which is consistent with previous findings [38]. It is possible that the sheet shape morphology is caused by the nature of the laminar structure. Clear fringes can be seen in Figure 4(d) with an interplanar distance of 4.57 nm, which corresponds to the plane of (120), and an interplanar distance of 5.76 nm

(a)

(b)

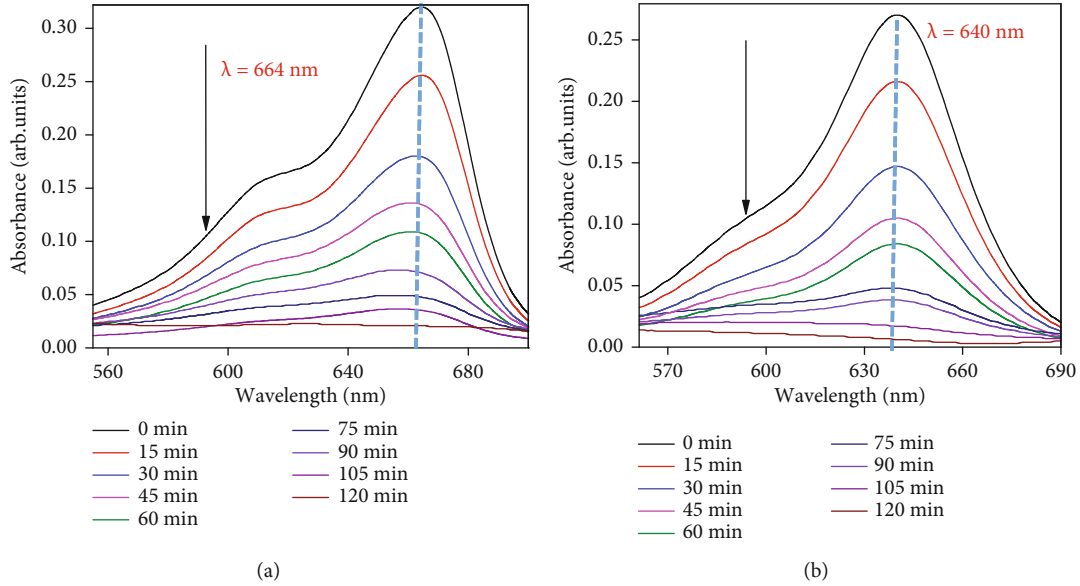FIGURE 6: (a) and (b) Absorption spectra of MB and AR dyes decomposition for Bi_2O_3 NPs.
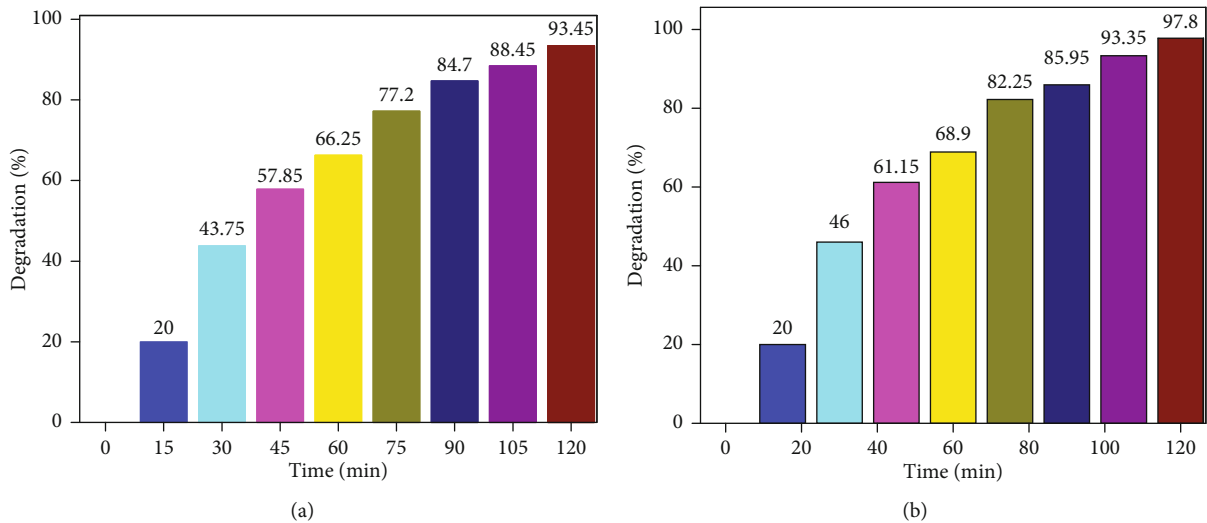

(a)

(b)

FIGURE 7: (a) and (b) Plot of C/C_o for the decolorization of MB and AR under UV light illumination.

TABLE 4: Rate constants and kinetic studies of Bi_2O_3 for methylene blue (MB) decolorization under UV light irradiation.

	20 ppm MB + 60 mg Bi_2O_3 + UV light				
t	c	c/co	Log c/co	-log c/co	%D
0	20	1	0	0	0
15	16	0.8	-0.09691	0.09691	20
30	11.25	0.5625	-0.24988	0.249877	43.75
45	8.43	0.4215	-0.3752	0.375202	57.85
60	6.75	0.3375	-0.47173	0.471726	66.25
75	4.56	0.228	-0.64207	0.642065	77.2
90	3.06	0.153	-0.81531	0.815309	84.7
105	2.31	0.1155	-0.93742	0.937418	88.45
120	1.31	0.0655	-1.18376	1.183759	93.45

Rate = 0.018758 min^{-1}.

(Figure 4(c)), which corresponds to the plane of (-122). The other planes, which are denoted by the numbers 3 and 4 in the SAED pattern of prepared Bi_2O_3, correspond to the planes of (112) and (041). The planes observed in the SAED pattern are in excellent agreement with the planes observed in the XRD pattern.

3.5. Diffuse Reflectance Spectroscopy (DRS) Analysis. The value of E_g for Bi_2O_3 NPs was evaluated by using the UV–vis reflectance spectroscopy is given in Figure 5 [39]. The synthesized NPs exhibited a representative reflectance with a strong transition in the UV region corresponding to the bandgap transition of the Bi_2O_3 semiconductor. The Kubelka-Munk function F(R) provides the diffused reflectance as a function of absorption coefficient and can be utilized for examining the powders as given by the following equation:
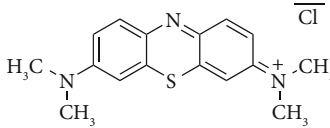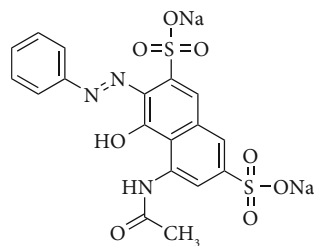
TABLE 5: List of dyes.

Name of dye	Type of dye	Class of dye	Structure	Mol.wt (g/mol)
Methylene blue	Basic dye	Thiazine		319.9
Acid red	Acid dye	Azo dye		400.38

TABLE 6: Rate constants and kinetic studies of Bi_2O_3 for acid red (AR) decolorization under UV light irradiation.

		20 ppm AR + 60 mg Bi_2O_3 + UV light			
t	c	c/co	Log c/co	-log c/co	%D
0	20	1	0	0	0
15	16	0.8	-0.09691	0.09691	20
30	10.8	0.54	-0.26761	0.267606	46
45	7.77	0.3885	-0.41061	0.410609	61.15
60	6.22	0.311	-0.50724	0.50724	68.9
75	3.55	0.1775	-0.7508	0.750802	82.25
90	2.81	0.1405	-0.85232	0.852324	85.95
105	1.33	0.0665	-1.17718	1.177178	93.35
120	0.44	0.022	-1.65758	1.657577	97.8

Rate = 0.020392 min^{-1}.

$$F(R) = \frac{(1-R)^2}{2R}, \tag{10}$$

where R is reflectance and $F(R)$ is Kubelka-Munk functions.

The inset of Figure 5 shows the direct bandgap energy was estimated by plotting $[f(R)(hv)]^2$ vs. energy gap (eV). The optical energy gap was calculated using the Tauc relation [40], as given by the following equation.

$$(\alpha hv) = A (hv - Eg)^n, \tag{11}$$

where hv; photon energy, α; absorption coefficient ($\alpha = 4\pi k/\lambda$); (k; absorption index or absorbance, λ; the wavelength in nanometer), Eg; energy band gap, A; constant, n = 1/2 for the allowed direct bandgap. The exponent "n" depends on the type of transition, and it may have values 1/2, 2, 3/2, and 3 corresponding to the allowed direct, allowed indirect, forbidden direct, and forbidden indirect transitions, respectively [41, 42]. The optical energy gap thus calculated for the synthesized Bi_2O_3 NPs is 3.3 eV and is shown in the inset of Figure 5. This resulted in the genera-

tion of higher electron-hole pairs for better photocatalytic efficiency.

3.6. Photocatalytic Studies. Spherical glass reactor with 176.6 cm^2 surface areas and mercury vapor lamps UV light source with 125 W medium pressures were used to carry out photocatalytic experiments. The emission wavelength with the highest emission at 370 nm (UVA) in the range of 350–400 nm was utilized, and no filters were used to exclude the light of different wavelengths. In open-air conditions, at a distance of 23 cm, the light was directly irradiated onto the reaction mixture. Double distilled water was used to perform all the experiments. The experiment was conducted using 60 mg of photocatalyst sample Bi_2O_3 was dissolved in 250 mL of 20 ppm concentrated dye solution. Throughout the experiment, the solution was stirred continuously by using a magnetic stirrer. At definite time intervals, 5 mL of the reaction mixture was collected from the dye solution, and the catalyst particles were removed using an external magnet [43, 44].

Photocatalytic activity (PCA) of the Bi_2O_3 NPs was assessed by photodegradation of methylene blue (MB), a cationic dye with maximum absorption at 664 nm, and acid red (AR), an anionic dye with maximum absorption at 640 nm as shown in Figures 6(a) and 6(b). Initially, the PCA experiments were carried out in the dark condition to see the photocatalytic activity for (MB) and (AG) dye using the synthesized catalysts. The dyes did not undergo any degradation, and hence, no change was observed [45, 46].

As presented in Figures 7(a) and 7(b) after 120 min of UV light irradiation, the photodegradation rate of MB dye (Tables 4 and 5) was found to be 93.45%, but, in the same environment, the photodegradation rate of AR dye (Tables 6 and 5) was recorded to be 97.8%. This clearly indicates that AR dye is more susceptible to decolorization than MB when exposed to UV light for 120 min. The obtained results are superior compared to the earlier published work where the dye degradation efficiencies were found to be 95.02% for Fast Red acid dye [47] and 92.3 for methylene blue dye [48]. The percentage of degradation was calculated from the following equation,
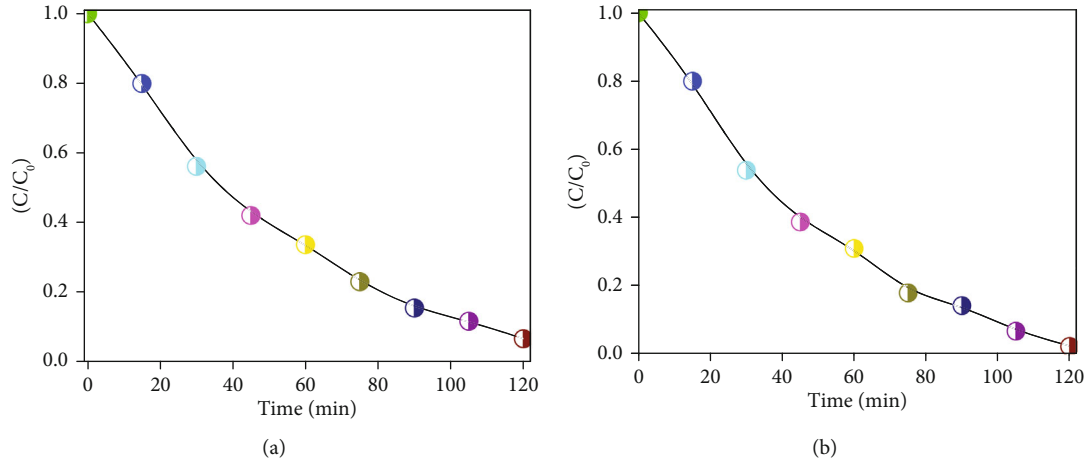
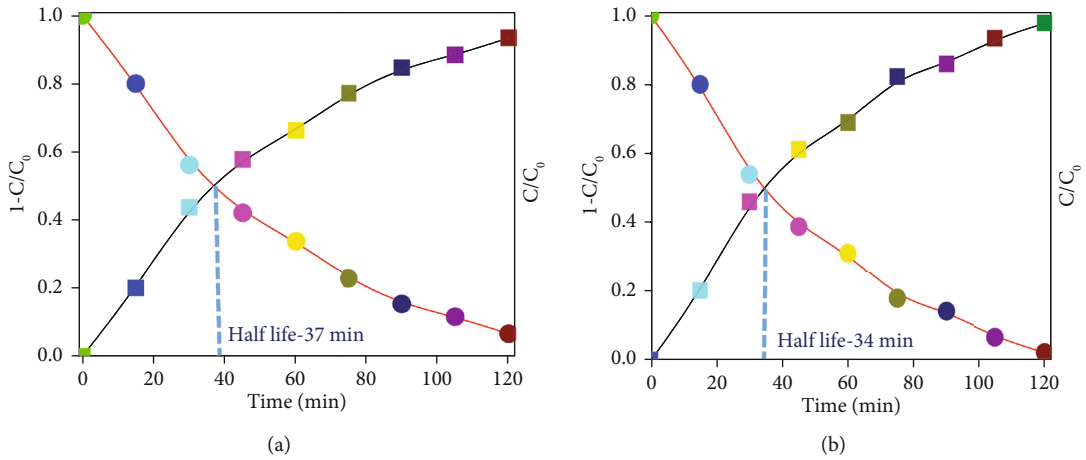FIGURE 8: (a) and (b) Percentage decomposition of MB and AR dyes over Bi_2O_3 NPs.

FIGURE 9: (a) and (b) Time span of MB and AR dyes over Bi_2O_3 NPs.

$$\%D = \frac{C_o - C}{C_o \times 100}, \qquad (12)$$

where %D is photo-decolorization efficiency, C_o and C are initial concentrations of the dye solutions and the residual concentration of the dye in solution after decolorization in equilibrium, respectively.

Langmuir-Hinshelwood kinetic model was utilized to discuss photocatalytic degradation Kinetics of MB and AR by Bi_2O_3 NPs as shown in Figures 8(a) and 8(b), using the following equation.

$$\log \frac{c}{C_o} = -Kt, \qquad (13)$$

where C_o is concentration of MB and AG dyes initially, C is concentration at time t, k is rate of first-order kinetics (min^{-1}), and t is time in seconds.

The slope of (log C/C_o) vs. time (t) gives the rate constant K. The rate constant values for Bi_2O_3 NPs are 0.018758 min^{-1} (MB) and 0.020392 min^{-1} (AG). First-order kinetics was confirmed from the values calculated from the direct relationship between log C/C_o and k.

In Figures 9(a) and 9(b), the degradation half-life was evaluated in which 50% dye degradation was observed in a time span of 37 min for (MB) and 34 min (AG). The results indicated that bismuth oxide is prominent material for the degradation of textile dye pollutants and is also useful for the removal of secondary pollutants. A novel bismuth oxide-based thin film as a photocatalyst recorded 98% degradation under UV light irradiation for 8 hours while obtaining a 73.47% COD (chemical oxygen) reduction. The photocatalytic degradation managed to degrade the smaller organic molecules that were formed during the initial stages of degradation, leaving behind the less decomposable by-products [49].

3.7. Mechanism of Photocatalytic Degradation. As the solution containing photocatalyst (Bi_2O_3 NPs) is irradiated by visible (Vis) radiation, electrons in the valence band (VB) of the catalyst get transferred to the conduction band (CB) by creating a hole in VB (Figure 10) [46]. These holes and electrons interact with H_2O and O_2 to yield OH• and O_2•⁻, respectively, and then the hydroxyl radicals interact with dye molecules to degrade to smaller molecules [50, 51]. The main steps involved in the reaction process of photocatalytic degradation under visible light irradiation are as follows:
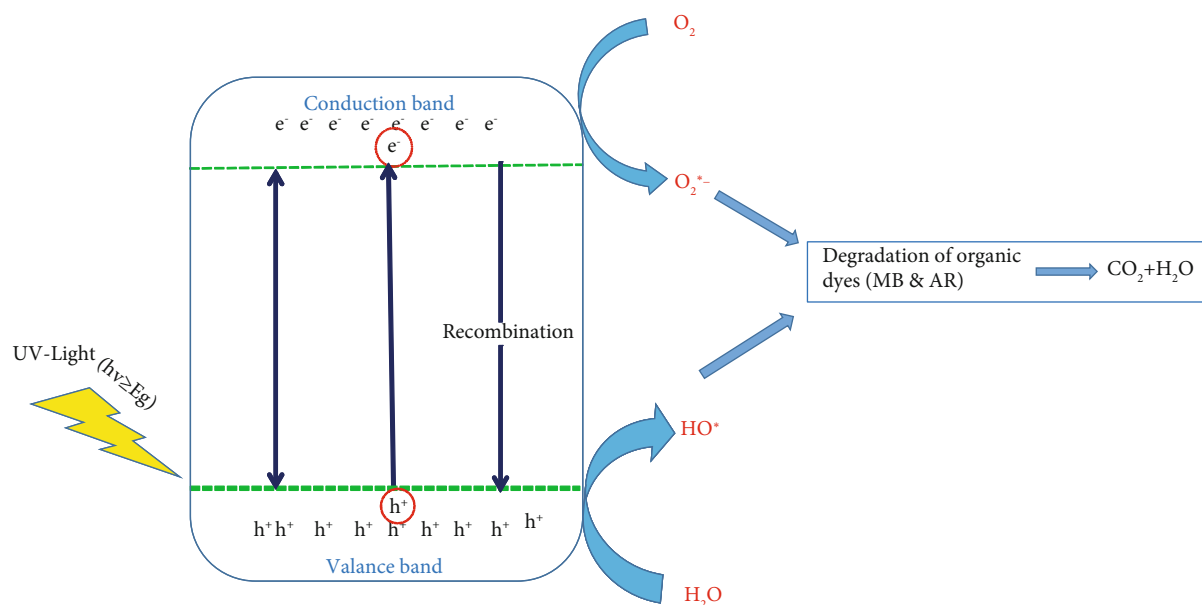
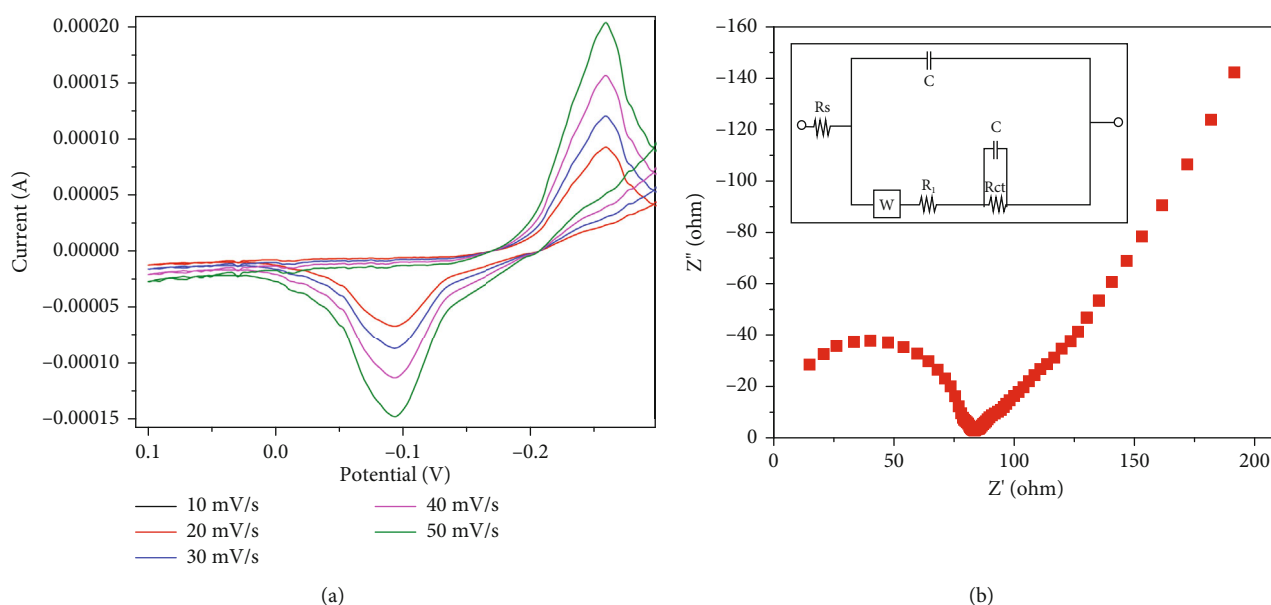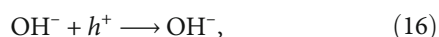FIGURE 10: The mechanism of MB and AR dyes decomposition for Bi_2O_3 NPs.

(a)

(b)
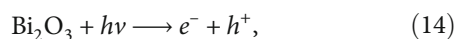
FIGURE 11: (a) Cyclic voltammogram of Bi_2O_3 NPs with different scanning rates. (b) EIS spectra with equivalent circuit of Bi_2O_3 NPs.

$$Bi_2O_3 + h\nu \longrightarrow e^- + h^+, \qquad (14)$$

$$O_2 + e^- \longrightarrow O_2, \qquad (15)$$

$$OH^- + h^+ \longrightarrow OH^-, \qquad (16)$$

$$OH^- + O_2^- + Dyes \longrightarrow Decomposed\ product. \qquad (17)$$

It contributed towards the practicality of the synthesized Bi_2O_3 NPs as they could be applied in the degradation of other organic pollutants.

3.8. Cyclic Voltammetric Studies. In order to characterize the synthesized Bi_2O_3 NPs based sensor, a variety of electrochemical measurements were performed in 0.1 M HCl using lead and ascorbic acid, including cyclic voltammetry (CV) and electrochemical impedance spectroscopy (EIS) (Figure 11). For the cyclic voltammetry studies of the synthesized Bi_2O_3, a standard three-electrode system in 0.1 M HCl was used. Using a scan rate ranging from 10 mV/s to 50 mV/s, this process was carried out in the absence of lead and/or ascorbic acid. It has been determined that the reduction and oxidation peaks observed at potentials of -0.25 V and -0.09 V, respectively, when the potential range was varied from -0.3 to +0.1, were caused by variations in the potential range from -0.3 to +0.1. With the help of cyclic voltammograms, the specific capacitance of the electrode (Fg^{-1}) could be calculated using the following equation,
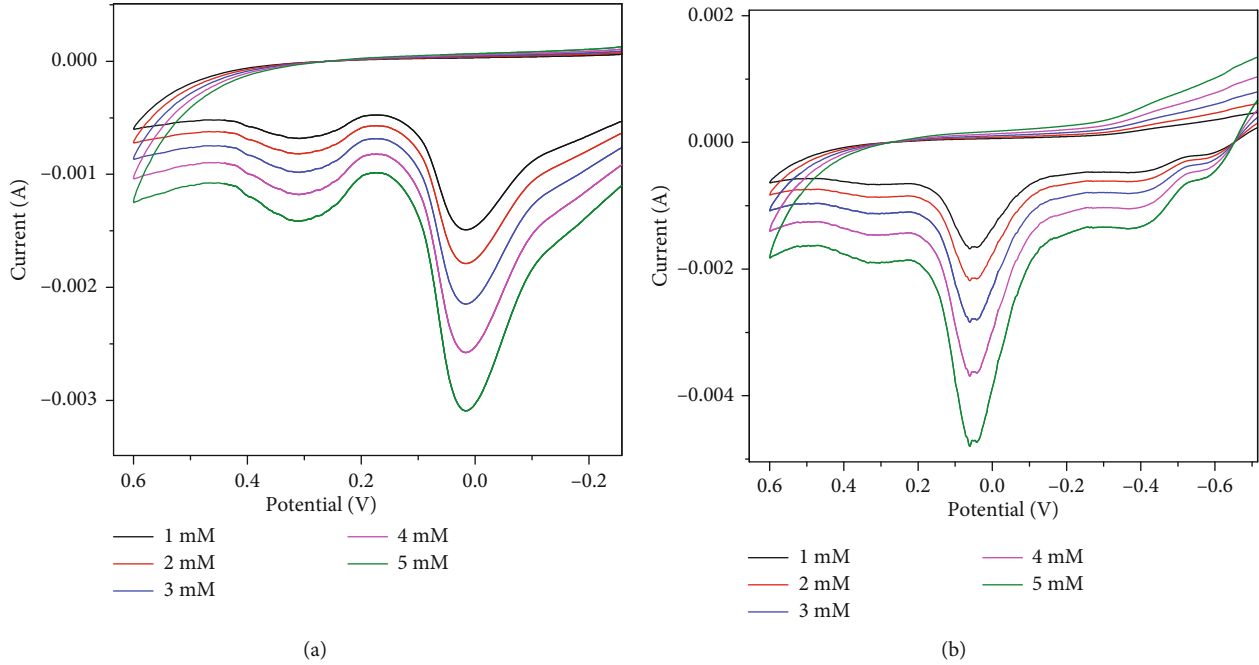
(a)

(b)

FIGURE 12: Cyclic voltammogram of Bi_2O_3 NPs. Detection of (a) ascorbic acid and (b) lead concentration range 1–5 mM.
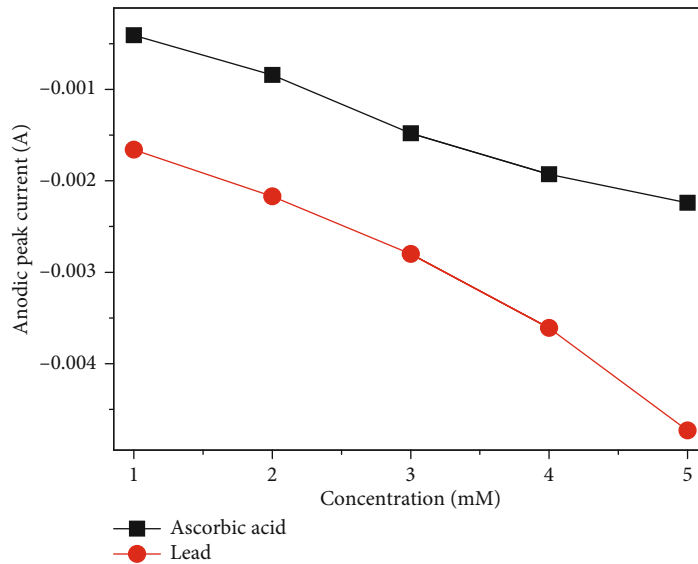

FIGURE 13: Anodic peak current vs. concentration plot using linear sweep voltammetry (LSV).

$$C_{sp} = \frac{S}{2mk\Delta V}. \tag{18}$$

The area under the CV curve can be represented by S, as given in equation (18), where the mass of the material was represented by m, voltage window was represented by ΔV, and scan rate was given by k. The specific capacitance values were calculated using equation (18) and were found to be 86.6, 55.7, 36.1, 29.8, and 25.5 Fg^{-1}, respectively, for scan rates of 10, 20, 30, 40, and 50 mV in 0.1 M HCl. It can be seen from the specific capacitance values that as the scan rate increases, the specific capacitance values decrease. This can be attributed to the fact that the ions in the electrolyte will have sufficient time to penetrate into the electrode material at a lower scan rate, whereas at a higher scan rate, the ions will simply collect on the electrode material's outer surface [52]. This results in a decrease in the values of specific capacitance as a result of an increase in scan rate as well [53].

The Nyquist plot (Figure 11(b)) can be used to determine the electronic conductivity or charge transfer capacity of the prepared electrode. This plot also provides information on the capacitance behavior of the electrode. It is possible to divide the Nyquist plot into two main regions: the first denotes the high-frequency region, which provides information about the charge transfer process at the interface of

electrode and/or electrolyte, which is typically seen as a semicircle [54, 55]. The other region represents the low-frequency region, which denotes the capacitance of the electrode and which was given the shape of a straight line in order to represent it accurately. The charge transfer resistance Rct was calculated from the diameter of the semicircle in the Nyquist plot [56]. When the EIS technique was used, it was possible to obtain the equivalent circuit of the system which was given in Figure 11(b) inset.

The sensing capability of the synthesized nanomaterial (Bi_2O_3) for ascorbic acid and lead was investigated using a modified carbon paste electrode, and the obtained results were presented in Figure 12. We experimented with different concentrations of ascorbic acid/lead from 1 to 5 mM in order to better understand the sensing ability of synthesized Bi_2O_3. According to the results, in the absence of ascorbic acid and lead, the oxidation and reduction peaks were at -0.09 V and -0.2 V, respectively, whereas in the presence of ascorbic acid and lead, the oxidation and reduction peaks shifted to the more positive side of the potential curve [57]. After the addition of ascorbic acid, the oxidation peak at -0.09 V shifts to 0.019 V, and an additional oxidation peak appears at 0.03 V, whereas when the lead is added, the oxidation peak at -0.09 V shifts to 0.05 V. After the addition of ascorbic acid/lead, there is a complete disappearance of the reduction peak in the voltammogram (Figure 12). We can infer from the data that the synthesized material Bi_2O_3 can function as a good sensing material for ascorbic acid and lead, which is supported by the significant variation in the oxidation and reduction peak positions of the material. Figure 13 shows the concentration of ascorbic acid and lead vs. anodic peak current plot obtained by LSV, which also shows an increase in anodic peak current with increasing concentration of ascorbic acid and lead.

4. Conclusions

To summarize, in this research, we have used a well-known probe sonication approach for the synthesis of Bi_2O_3 nanoparticles that is low in cost and highly calibrated. The produced nanoparticles were submitted to a number of different characterization procedures in order to gain a better understanding of their crystal structure, as well as their morphological and optical characteristics. It was discovered from the optical properties of the Bi_2O_3 nanoparticles have a bandgap of 3.3 eV, which makes them excellent for the degradation of dyes when exposed to ultraviolet radiation. The SEM, TEM, and HRTEM analyses revealed that the nanoparticles are highly porous materials with a small agglomeration. MB and AR dyes were both subjected to degradation under ultraviolet (UV) radiation in the presence of the catalyst, and it was observed that the degradation of MB and AR dyes was 93.45% and 97.80%, respectively, and that the results were quite impressive. In the electrochemical investigations, it was discovered that the produced nanomaterial has the ability to detect several heavy metals as well as the ascorbic acid medication. The specific capacitance of the sample was calculated to be 25.5 Fg^{-1} in 0.1 N HCl, according to the results of

the experiment. Hence, Bi2O3 nanoparticles can be used as bifunctional materials for degradation and for sensing applications.

Data Availability

The [Excel] data used to support the findings of this study are available from the corresponding author upon request.

Conflicts of Interest

The authors declare that they have no conflicts of interest.

References

[1] H. M. Zaid, "Synthesis of bismuth oxide nano powders via electrolysis method and study the effect of change voltage on the size for it," *Australian Journal of Basic and Applied Sciences.*, vol. 11, pp. 97–101, 2017.

[2] N. Cornei, N. Tancet, F. Abraham, and O. Mentré, "Synthesis and characterization of bismuth oxide nanoparticles via sol-gel method inorganic chemistry," *Journal of Inorganic Chemistry*, vol. 3, 165 pages, 2006.

[3] A. Kumar, A. Rana, C. Guo et al., "Acceleration of photoreduction and oxidation capabilities of $Bi_4O_5I_2$/ alginate by metallic Ag: wide spectral removal of nitrate and azithromycin," *Chemical Engineering Journal*, vol. 423, article 130173, 2021.

[4] A. Kumar, G. Sharma, A. Kumari et al., "Construction of dual Z-scheme g-C3N4/Bi4Ti3O12/Bi4O5I2 heterojunction for visible and solar powered coupled photocatalytic antibiotic degradation and hydrogen production: boosting via I^-/I_3^- and Bi^{3+}/Bi^{5+} redox mediators," *Applied Catalysis B: Environmental*, vol. 284, article 119808, 2021.

[5] P. Dhiman, A. Kumar, M. Shekh et al., "Robust magnetic ZnO-Fe_2O_3 Z-scheme hetereojunctions with in-built metal-redox for high performance photo- degradation of sulfamethoxazole and electrochemical dopamine detection," *Environmental Research*, vol. 197, article 111074, 2021.

[6] A. Bouziani, J. Park, and A. Ozturk, "Effects of fluorination and thermal shock on the photocatalytic activity of Bi_2O_3 nanopowders," *Colloids and Surfaces A: Physicochemical and Engineering Aspects*, vol. 626, article 127049, 2021.

[7] A. P. Kumar, D. Bilehal, T. Desalegn et al., "Studies on synthesis and characterization of Fe3O4@SiO2@Ru hybrid magnetic composites for reusable photocatalytic application," *Adsorption Science & Technology*, vol. 2022, Article ID 3970287, 18 pages, 2022.

[8] B. Abebe and H. C. Ananda Murthy, "Synthesis and characterization of Ti-Fe oxide nanomaterials for lead removal," *Journal of Nanomaterials*, vol. 2018, Article ID 9651039, 10 pages, 2018.

[9] B. Abebe, E. A. Zereffa, and H. C. A. Murthy, "Synthesis of poly(vinyl alcohol)-aided ZnO/Mn2O3 nanocomposites for acid orange-8 dye degradation: mechanism and antibacterial activity," *ACS Omega*, vol. 6, no. 1, pp. 954–964, 2021.

[10] B. Abebe, H. C. A. Murthy, E. A. Zereffa, and Y. Qiang, "Synthesis and characterization of PVA-assisted metal oxide nanomaterials: surface area, porosity, and electrochemical property improvement," *Journal of Nanomaterials*, vol. 2020, Article ID 6532835, 14 pages, 2020.

[11] B. Abebe, C. R. Ravikumar, E. A. Zereffa, A. Naveen Kumar, and H. C. A. Murthy, "Photocatalytic and superior ascorbic acid sensor activities of PVA/Zn-Fe-Mn ternary oxide nanocomposite," *Inorganic Chemistry Communications*, vol. 123, article 108343, 2021.

[12] G. Viruthagiri, P. Kannan, and V. K. Indhumathi, "Photocatalytic activity of α-phase bismuth oxide nanoparticles under visible light," *International Journal of Advanced Science and Research*, vol. 2, pp. 1–7, 2017.

[13] B. Abebe, E. A. Zereffa, H. C. A. Murthy, and C. R. Ravikumar, "A novel poly (vinyl alcohol)-aided ZnO/Fe2O3 nanocomposite as an ascorbic acid sensor," *Journal of Materials Science: Materials in Electronics*, vol. 32, no. 6, pp. 7778–7790, 2021.

[14] M. R. A. Kumar, B. Abebe, H. P. Nagaswarupa, H. C. A. Murthy, C. R. Ravikumar, and F. K. Sabir, "Enhanced photocatalytic and electrochemical performance of TiO_2-Fe2O3 nanocomposite: its applications in dye decolorization and as supercapacitors," *Scientific Reports*, vol. 10, no. 1, p. 1249, 2020.

[15] M. Ahmed, A. Dief, and W. S. Mohamed, "α-Bi_2O_3 nanorods: synthesis, characterization and UV-photocatalytic activity," *Materials Research Express*, vol. 4, pp. 35–39, 2017.

[16] L. Liu, J. Jiang, S. Jin, Z. Xiabc, and M. Tangc, "Hydrothermal synthesis of β-bismuth oxide nanowires from particles," *CrystEngComm*, vol. 13, pp. 25–29, 2011.

[17] Z. Hamid, "Synthesis of bismuth oxide nano powders via electrolysis method and study the effect of change voltage on the size for it," *Australian journal of basic and applied sciences*, vol. 7, pp. 97–101, 2017.

[18] T. R. Das, S. Patra, R. Madhuri, and K. P. Sharma, "Bismuth oxide decorated graphene oxide nanocomposites synthesized via sonochemical assisted hydrothermal method for adsorption of cationic organic dyes," *Journal of colloid and interface science*, vol. 509, pp. 82–93, 2018.

[19] M. M. Patil, V. V. Deshpande, S. R. Dhage, and V. Ravi, "Synthesis of bismuth oxide nanoparticles at 100 °C," *Materials letters*, vol. 59, no. 19-20, pp. 2523–2525, 2005.

[20] D. Sánchez-Martínez, I. Juárez-Ramírez, L. M. Torres-Martínez, and I. de León-Abarte, "Photocatalytic properties of Bi_2O_3 powders obtained by an ultrasound-assisted precipitation method," *Ceramics International*, vol. 42, no. 1, pp. 2013–2020, 2016.

[21] Y. Astuti, A. Fauziyah, S. Nurhayati et al., "Synthesis of α-bismuth oxide using solution combustion method and its photocatalytic properties," *IOP Conference Series: Materials Science and Engineering*, vol. 107, article 012006, 2016.

[22] N. M. Sammes, G. A. Tompsett, H. Näfe, and F. Aldinger, "Bismuth based oxide electrolytes– structure and ionic conductivity," *Journal of the European Ceramic Society*, vol. 19, no. 10, pp. 1801–1826, 1999.

[23] Y. Dimitriev, M. Y. Krupchanska Ivanova, and A. Staneva, "Sol-gel synthesis of material in the system Bi2O3-SiO2," *Journal of the University of Chemical Technology and Metallurgy*, vol. 45, pp. 39–42, 2010.

[24] J. Y. Xia, M. T. Tang, C. H. Cui, S. M. Jin, and Y. M. Chen, "Preparation of α- Bi2O3 from powders through low temperature oxidation," *Transactions of Nonferrous Metals Society of China*, vol. 22, pp. 2289–2294, 2012.

[25] H. Kim, J. Kim, W. Kim, and W. Choi, "Enhanced photocatalytic and photoelectrochemical activity in the ternary hybrid of CdS/TiO2/WO3through the cascadal electron transfer," *The Journal of Physical Chemistry C*, vol. 115, no. 19, pp. 9797–9805, 2011.

[26] N. Cornei, N. Tancet, F. Abraham, and O. Mentré, "Synthesis and characterization of bismuth oxide nanoparticles via sol-gel method," *Inorganic Chemistry*, vol. 3, pp. 162–165, 2006.

[27] N. Jiang and E. D. Wachsman, "Structural stability and conductivity of phase-stabilized cubic bismuth oxides," *Journal of the American Ceramic Society*, vol. 82, no. 11, pp. 3057–3064, 1999.

[28] M. Zidan, "Electrochemical oxidation of paracetamol mediated by nanoparticles bismuth oxide modified glassy carbon electrode," *International Journal of Electrochemical Science*, vol. 6, pp. 279–288, 2011.

[29] M. Mallahi, A. Shokuhfar, M. R. Vaezi, A. Esmaeilirad, and V. Mazinani, "Synthesis and characterization of bismuth oxide nanoparticles via sol-gel method," *Journal of Engineering Research (AJER)*, vol. 3, pp. 162–165, 2014.

[30] M. A. S. Amulya, H. P. Nagaswarupa, M. R. A. Kumar, C. R. Ravikumar, and K. B. Kusuma, "Sonochemical synthesis of $MnFe_2O_4$ nanoparticles and their electrochemical and photocatalytic properties," *Journal of Physics and Chemistry of Solids*, vol. 148, article 109661, 2021.

[31] M. W. Alam, V. G. Dileep Kumar, C. R. Ravikumar, S. C. Prashantha, H. C. Ananda Murthy, and M. R. Anil Kumar, "Chromium (III) doped polycrystalline MgAl2O4 nanoparticles for photocatalytic and supercapacitor applications," *Journal of Physics and Chemistry of Solids*, vol. 161, p. 110491, 2022.

[32] C. R. Ravi Kumar, M. S. Santosh, H. P. Nagaswarupa, S. C. Prashantha, S. Yallappa, and M. R. Anil Kumar, "Synthesis and characterization ofβ-Ni(OH)2embedded with MgO and ZnO nanoparticles as nanohybrids for energy storage devices," *Materials Research Express*, vol. 4, no. 6, article 065503, 2017.

[33] A. Yamuna, P. Sundaresan, and S. M. Chen, "Sonochemical preparation of bismuth oxide nanotiles decorated exfoliated graphite for the electrochemical detection of imipramine," *Ultrasonics sonochemistry*, vol. 64, article 105014, 2020.

[34] M. G. Naseri, E. B. Saion, H. A. Ahangar, and A. H. Shaari, "Fabrication, characterization, and magnetic properties of copper ferrite nanoparticles prepared by a simple, thermal-treatment method," *Materials Research Bulletin*, vol. 48, no. 4, pp. 1439–1446, 2013.

[35] T. Saison, N. Chemin, C. Chaneac et al., "Bi2O3, BiVO4, and Bi2WO6: impact of surface properties on photocatalytic activity under visible light," *The Journal of Physical Chemistry C*, vol. 115, no. 13, pp. 5657–5666, 2011.

[36] S. Nandi and S. K. Das, "An electrochemical study on bismuth oxide (Bi_2O_3) as an electrode material for rechargeable aqueous aluminum-ion battery," *Solid State Ionics*, vol. 347, article 115228, 2020.

[37] J. Feng, L. Q. Guo, X. D. Xu, S. Y. Qi, and M. L. Zhang, "Hydrothermal synthesis and characterization of $Mn_{1-x}Zn_xFe_2O_4$ nanoparticles," *Physica B: Condensed Matter*, vol. 394, no. 1, pp. 100–103, 2007.

[38] T. Liu, Y. Zhao, L. Gao, and J. Ni, "Engineering Bi_2O_3-Bi_2S_3 heterostructure for superior lithium storage," *Scientific Reports*, vol. 5, no. 1, pp. 1–5, 2015.

[39] P. Kubelka and F. M. Aussig, "Ein beitrag zur optik der farbanstriche," *Zeitschrift fur technische Physik*, vol. 12, pp. 593–601, 1931.

[40] M. Stucchi, C. L. Bianchi, C. Argirusis et al., "Ultrasound assisted synthesis of Ag-decorated TiO_2 active in visible light," *Ultrasonics Sonochemistry*, vol. 40, no. Part A, pp. 282–288, 2018.

[41] Y.-C. Chu, G.-J. Lee, C.-Y. Chen et al., "Preparation of bismuth oxide photocatalyst and its application in white-light LEDs," *Journal of Nanomaterials*, vol. 2013, Article ID 596324, 7 pages, 2013.

[42] K. Rana, P. Thakur, P. Sharma, M. Tomar, V. Gupta, and A. Thakur, "Improved structural and magnetic properties of cobalt nanoferrites: influence of sintering temperature," *Ceramics International*, vol. 41, no. 3, pp. 4492–4497, 2015.

[43] Q. R. Deng, X. H. Xia, M. L. Guo, Y. Gao, and G. Shao, "Mn-doped TiO2 nanopowders with remarkable visible light photocatalytic activity," *Materials Letters*, vol. 65, no. 13, pp. 2051–2054, 2011.

[44] M. R. A. Kumar, C. R. Ravikumar, H. P. Nagaswarupa et al., "Evaluation of bi-functional applications of ZnO nanoparticles prepared by green and chemical methods," *Journal of Environmental Chemical Engineering*, vol. 7, no. 6, article 103468, 2019.

[45] M. Chireh and M. Naseri, "Effect of calcination temperature on the physical properties of $LiFe_5O_8$ nanostructures," *Advanced Powder Technology*, vol. 30, no. 5, pp. 952–960, 2019.

[46] M. R. A. Kumar, H. P. Nagaswarupa, C. R. Ravikumar, S. C. Prashantha, H. Nagabhushana, and A. S. Bhatt, "Green engineered nano MgO and ZnO doped with Sm3+: synthesis and a comparison study on their characterization, PC activity and electrochemical properties," *Journal of Physics and Chemistry of Solids*, vol. 127, pp. 127–139, 2019.

[47] Y. Kambalagere, M. Madhusudana, and K. M. Mahadevan, "Decolourization of fast red acid dye using photoactive Bi_2O_3 nanoparticle under solar irradiation," in *Proceedings of the International Conference on Future Environment Pollution and Prevention (ICFEPP)*, pp. 11–16, Beijing, China, 2019.

[48] N. Nurmalasari, Y. Yulizar, and D. O. Apriandanu, "Bi2O3 nanoparticles: synthesis, characterizations, and photocatalytic activity," in , Article ID 0120363rd *International Symposium on Current Progress in Functional Materials*, vol. 763, Depok, Indonesia, 2020.

[49] L. Zhang, W. Wang, J. Yang et al., "Sonochemical synthesis of nanocrystallite Bi_2O_3 as a visible-light-driven photocatalyst," *Applied Catalysis A: General*, vol. 308, pp. 105–110, 2006.

[50] A. Tadesse, M. Hagos, N. Belachew, H. C. Ananda Murthy, and K. Basavaiah, "Enhanced photocatalytic degradation of Rhodamine B, antibacterial and antioxidant activities of green synthesised ZnO/N doped carbon quantum dot nanocomposites," *New Journal of Chemistry*, vol. 45, no. 46, pp. 21852–21862, 2021.

[51] Y. Yao, F. Lu, Y. Zhu et al., "Magnetic core-shell $CuFe_2O_4@C_3N_4$ hybrids for visible light photocatalysis of orange II," *J. Hazard.Mater.*, vol. 297, pp. 224–233, 2015.

[52] B. Shruthi, B. J. Madhu, V. B. Raju et al., "Synthesis, spectroscopic analysis and electrochemical performance of modified _β_ -nickel hydroxide electrode with CuO," *Journal of Science: Advanced Materials and Devices*, vol. 2, no. 1, pp. 93–98, 2017.

[53] K. B. Kusuma, M. Manju, C. R. Ravikumar et al., "Photocatalytic and electrochemical sensor for direct detection of paracetamol comprising γ-aluminium oxide nanoparticles synthesized via sonochemical route," *Sensors International*, vol. 1, article 100039, 2020.

[54] C. Pratapkumar, S. C. Prashantha, H. Nagabhushana et al., "White light emitting magnesium aluminate nanophosphor: near ultra violet excited photoluminescence, photometric characteristics and its UV photocatalytic activity," *Journal of Alloys and Compounds.*, vol. 728, pp. 1124–1138, 2017.

[55] Y. Wu, S. Liu, H. Wang, X. Wang, X. Zhang, and G. Jin, "A novel solvothermal synthesis of Mn_3O_4/graphene composites for supercapacitors," *Electrochimica Acta*, vol. 90, pp. 210–218, 2013.

[56] A. S. Manjunatha, N. S. Pavithra, M. Shivanna, G. Nagaraju, and C. R. Ravikumar, "Synthesis of Citrus Limon mediated SnO2-WO3 nanocomposite: applications to photocatalytic activity and electrochemical sensor," *Journal of Environmental Chemical Engineering*, vol. 8, no. 6, article 104500, 2020.

[57] C. R. Ravi kumar, P. Kotteeswaran, V. B. Raju et al., "Influence of zinc additive and pH on the electrochemical activities of β-nickel hydroxide materials and its applications in secondary batteries," *Journal of Energy Storage*, vol. 9, pp. 12–24, 2017.